

Magnetic rotation spectroscopy of molecular oxygen with a diode laser

R. J. Brecha, L. M. Pedrotti, and D. Krause

Department of Physics, University of Dayton, Dayton, Ohio 45469-2314

Received January 1, 1997; revised manuscript received April 9, 1997

The results of a study of molecular oxygen by magnetic rotation spectroscopy are presented. The experiment is based on the use of a semiconductor diode laser operating near room temperature at $\lambda = 762$ nm. The dependence of the signal on a variety of parameters including magnetic-field strength, oxygen pressure, and analyzing polarizer offset angle is investigated both theoretically and experimentally. © 1997 Optical Society of America [S0740-3224(97)01408-2]

1. INTRODUCTION

For many years magnetic rotation spectroscopy (MRS) has been used in investigations of paramagnetic molecular species.¹ In principle MRS is more sensitive than absorption spectroscopy and has the added characteristic of being selective of paramagnetic species only. An early series of papers on MRS described the spectroscopy of various vibrational bands of NO.²⁻⁷ That NO was initially chosen seems to have been incidental; the technique itself and comparison of theory with experiment were of paramount importance. More recently, sensitive detection of NO has been of greater interest as awareness of its role in atmospheric chemical processes has increased. Blake *et al.*⁸ have made a careful quantitative study of a magnetic rotation spectrometer capable of making *in situ* measurements of atmospheric NO concentration.

In addition, there have been studies of magnetic circular birefringence and dichroism effects in other species such as ICl (Ref. 9) and, by use of an extension of MRS to include frequency modulation, of PdH, PdD, NiH, and CuH.^{10,11} One reference in particular is oriented toward the pedagogical purpose of demonstrating how MRS can be used to simplify complex molecular spectra.¹² Curiously, however, one of the best-known paramagnetic species, diatomic oxygen, to the best of our knowledge has not been the subject of investigation by this technique. In this paper we present a study of magnetic rotation spectroscopy in O₂, using the so-called atmospheric band at $\lambda \sim 760$ nm. Given the importance of oxygen in combustion studies, for example, another sensitive detection technique could be of some practical interest. Our aim in the present study is to present a comparison of a simple theoretical model and experimental results, using a magnetic rotation spectrometer based on a semiconductor diode laser operating near room temperature.

MRS is based on the change in the state of the polarization of light that is due to the passage of the light through a gas cell immersed in a longitudinal magnetic field. One can monitor this change by placing the gas cell between two polarizers and detecting the light transmitted by the system. An experimental schematic is shown in Fig. 1. There are two contributors to the change in po-

larization state, magnetic circular birefringence (MCB) and magnetic circular dichroism (MCD). MCB (sometimes referred to as magnetic optical rotation) arises from the different indices of refraction of the gas for left and right circularly polarized (LCP and RCP, respectively) light. Linearly polarized light, made up of RCP and LCP components, will experience a rotation of the plane of polarization during its passage through the cell. The absorption coefficients for LCP and RCP light also differ for a paramagnetic gas in a magnetic field; thus, after passing through the sample, light that is initially linearly polarized will in general be elliptically polarized.

Qualitative examples of MRS signals are illustrated in Fig. 2. Figure 2(a) shows an energy-level diagram for a transition between molecular angular momentum states with $J = 1$ (magnetic sublevels $m = -1, 0, +1$) and $J = 0$ ($m = 0$). With no magnetic field applied, the lower-state energies are degenerate. As we are interested in the situation in which linearly polarized light is incident, we have illustrated the respective absorption transitions for RCP (σ_+) light, which drives only the transition $m = -1 \rightarrow m = 0$, and LCP (σ_-) light, which drives only the transition $m = +1 \rightarrow m = 0$. We plot in Fig. 2(c) the indices of refraction n_+ for RCP light and $-n_-$ for LCP light as a function of frequency. The MCB signal will be shown to be dependent on the relative phase shifts experienced by RCP and LCP light and thus on the difference between n_+ and n_- . The net signal in this case is simply zero, the sum of the two curves shown in Fig. 2(c). For an applied magnetic field the energy-level degeneracy for $m = \pm 1$ is lifted, splitting the energy levels by an amount δ , as shown in Fig. 2(b). This split leads to a shift in frequency of the respective index of refraction curves, illustrated in Fig. 2(d). The MCB signal is then as shown, with the maximum rotation of polarization occurring at the original unperturbed transition frequency.

MCD can be qualitatively explained by similar arguments. In Fig. 2(e) we plot the absorption coefficients α_+ and $-\alpha_-$ for zero applied magnetic field. Again, the signal for MCD depends on the difference between the two and for zero applied field vanishes. With an applied

B field the absorption peaks shift in opposite directions, and the difference of the absorption coefficients gives the curve shown in Fig. 2(f). For any real system there will be a more-or-less complicated combination of the two above-mentioned effects. In Section 2 we present a detailed discussion applicable to our experiment.

Finally, in Figs. 2(g) and 2(h) we show the first derivative of the curves in Figs. 2(d) and 2(f), respectively. The phase-sensitive detection used in the experiment described below leads to a signal that is the derivative with

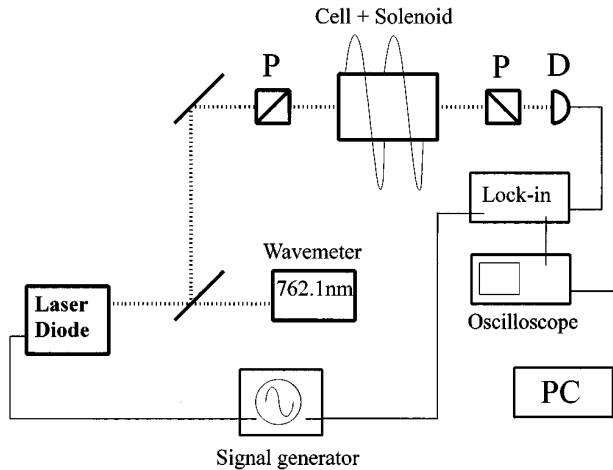


Fig. 1. Schematic of the experimental setup used for magnetic rotation spectroscopy. The important elements include the laser diode; two polarizers (P's), the second of which can be rotated an angle of θ measured with respect to the position at which the two polarizers are crossed; a gas cell immersed in the longitudinal magnetic field produced by a long tightly wrapped solenoid; the detector (D); and the data analysis system [lock-in amplifier, oscilloscope, and computer (PC)].

respect to frequency of the intensity at the detector. In what follows we will be referring to the derivatives in all discussions of theoretical and experimental results.

In this paper we concentrate on the oxygen absorption band $b^1\Sigma_g^+ - X^3\Sigma_g^-$ which is an $N = 0 \leftarrow N = 1$ transition as discussed above. We have investigated the dependence of MRS signals on magnetic-field strength, polarizer offsets, and oxygen pressure. The question of ultimate detection capabilities and quantitative extraction of molecular parameters is deferred to future research.

The oxygen transition of interest is doubly weak. First, it is a magnetic dipole transition and thus is roughly 5 orders of magnitude weaker than a normal electric dipole transition. Second, the transition is a singlet-triplet intercombination band, making it 3 orders of magnitude weaker still. In spite of the weakness of the transition, this band has been well studied, and absorption signals are easily detectable for a path length of a fraction of a meter at atmospheric pressure in room air.

2. THEORETICAL ANALYSIS

A. Modeling Magnetic Rotation Spectroscopy

The wave equation that governs the passage of an electromagnetic field through a gas cell in which the largest interaction has magnetic dipole character is

$$\nabla^2 \mathbf{E} - \frac{1}{c^2} \frac{\partial^2 \mathbf{E}}{\partial t^2} = \mu_0 \frac{\partial}{\partial t} (\nabla \times \mathbf{M}). \quad (1)$$

Here, \mathbf{E} is the electric field of the propagating wave, μ_0 is the permeability of free space, c is the speed of light in the gas, and \mathbf{M} is the magnetization of the gas sample. It is formed as a product of the number of molecules N per

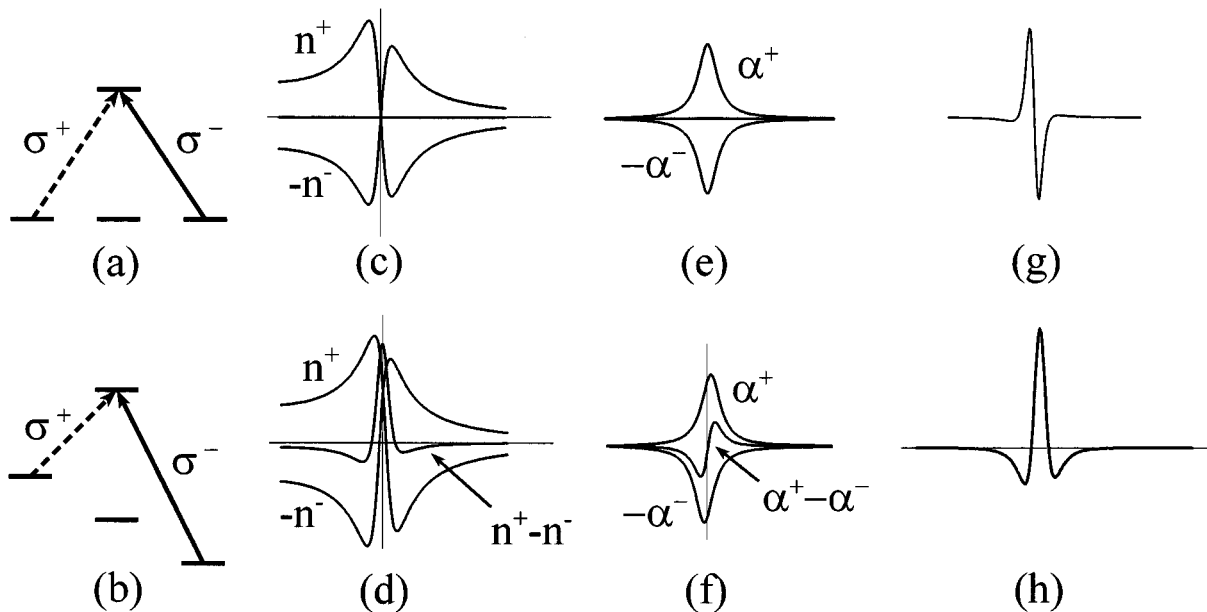


Fig. 2. Qualitative description of the two effects present in this system, MCB and MCD, and their characteristic signals. In (a) we sketch the energy levels for a simple $J = 1 \rightarrow J = 0$ transition with no applied field, and in (b) the same levels are shown with a B field applied. The $J = 1$ level splits into three sublevels, which are shifted (Zeeman effect). The resulting difference between n_R and n_L (MCB signal) is shown without and with the applied field in (c) and (d), respectively. In (e) and (f) we likewise show the difference between κ_R and κ_L (MCD signal) without and with the magnetic field, respectively. Finally, we show the first derivatives of the the MCB and the MCD signals in (g) and (h), respectively.

unit volume of the gas and the expectation value of the magnetic dipole moment of the molecule $\langle \mu \rangle$ for the near-resonant transition. The static magnetic field in the oxygen cell causes a Zeeman splitting of levels of the oxygen molecule nearly resonant with the driving electromagnetic field. This in turn causes differing absorptions and phase shifts for RCP and LCP light passing through the cell. It is convenient, therefore, to decompose the electric field that passes the first polarizer and emerges from the oxygen cell into RCP and LPC components as

$$\mathbf{E} = E_L \hat{e}_L \exp[-i(\omega t - kz + \phi_L)] + E_R \hat{e}_R \exp[-i(\omega t - kz + \phi_R)] + \text{c.c.} \quad (2)$$

Here,

$$\hat{e}_L = 1/2(\hat{x} - i\hat{y}), \\ \hat{e}_R = 1/2(\hat{x} + i\hat{y}).$$

Note that for $E_L = E_R$ and $\phi_L = \phi_R$, Eq. (2) represents light polarized along the x direction. We consider the second polarizer to be set to pass light that is linearly polarized along a direction making an angle θ with the y axis. The intensity of light that passes the second polarizer and reaches the detector takes the form

$$I = 1/2\epsilon_0 c \{E_L^2 + E_R^2 - 2E_L E_R \cos[2\theta - (\phi_R - \phi_L)]\}. \quad (3)$$

The intensity at the detector will vanish for $E_L = E_R$, $\phi_L = \phi_R$, and $\theta = 0^\circ$. Any intensity that does arrive at the detector after passing through the crossed polarizers is either a consequence of the different interactions of the LCP and RCP portions of the beam with the oxygen gas or is due to imperfections in the polarizers. In our model these effects are incorporated into Eq. (2) with the following definitions:

$$E_L = E_0 \exp(-\kappa g_L) + d/2, \\ E_R = E_0 \exp(-\kappa g_R) - d/2, \\ \phi_{L,R} = \kappa f_{L,R}.$$

The parameter

$$\kappa = \frac{N\mu_0\mu^2c\alpha}{2\hbar} l$$

is a measure of the strength of interaction of the laser light with the oxygen gas. In the definition of κ , N represents the total number density of molecules in the sample, μ is the magnetic dipole matrix element coupling the levels, α is the initial population probability of the lower atomic levels, l is the length of the oxygen cell, and the parameter d accounts for imperfect polarizers. The remaining amplitude decay and phase-rotation factors emerge from first-order time-dependent perturbation theory as (see Appendix A)

$$f_{L,R} = \int_{-\infty}^{\infty} \frac{1}{\sqrt{\pi}\Delta\omega} \exp[-(\omega' - \omega_{R,L})^2/\Delta\omega^2] \\ \times \frac{\omega(\omega - \omega')}{\gamma^2 + (\omega - \omega')^2} d\omega', \quad (4a)$$

$$g_{L,R} = \int_{-\infty}^{\infty} \frac{1}{\sqrt{\pi}\Delta\omega} \exp[-(\omega' - \omega_{R,L})^2/\Delta\omega^2] \\ \times \frac{\omega\gamma}{\gamma^2 + (\omega - \omega')^2} d\omega'. \quad (4b)$$

The Zeeman splitting is δ , and we define $\omega_{R,L} = \omega_0 \pm \delta$. Equations (4) include the effects of both inhomogeneous Doppler broadening and homogeneous pressure broadening (see Appendix A). The integrals in Eqs. (4) are related to the plasma dispersion function¹³ and can be evaluated numerically. In these results the homogeneous full width at half-maximum is 2γ and the width of the Doppler distribution is

$$2\sqrt{\ln(2)}\Delta\omega = \{4\pi[2\ln(2)kT/m]^{1/2}\}/\lambda,$$

where T is the temperature of the sample, k is Boltzmann's constant, and m is the mass of the oxygen molecule. At room temperature the Doppler width is $\sim 10^9$ Hz. The square of the ratio d/E_0 is the intensity extinction ratio of the crossed polarizers.

The phase-sensitive detection scheme used in the experiment produces a signal that is proportional to the derivative, with respect to the frequency of the driving field ω , of the intensity at the detector. Thus for all theoretical curves presented in this paper we show that the first derivative of the actual magnetic rotation signal will permit more direct comparison with experimental results. In addition, each theoretical trace represents the signal at zero magnetic field subtracted from that at a given magnetic-field strength, again to permit direct comparison with the experimental traces.

Two interesting limiting regimes are the cases for which the angle offset θ is zero and that for which θ is larger than both the differential phase shift caused by the presence of the magnetic field and the ratio d/E_0 . In the first case, for small κ , the signal reduces to

$$\frac{dI}{d\omega} \approx \frac{d}{d\omega} [I_0(d/2E_0)\kappa(g_L - g_R)],$$

whereas in the second case we find that

$$\frac{dI}{d\omega} \approx \frac{d}{d\omega} [2I_0\kappa\theta(f_L - f_R)].$$

Note that in the first of these cases the signal at the detector is proportional to the differential absorption, whereas in the second case the transmitted signal is proportional to the differential phase shift. These two cases thus correspond to MCD and the MCB as discussed in Section 1. The full form of the transmitted signal was used to produce all the theoretical plots in this paper. Note also that direct probing of the MCB signal is possible only for an analyzer setting of $\theta = 0^\circ$. Finally, for $\theta = 0^\circ$ the lowest-order contribution to the transmitted signal is proportional to the field extinction coefficient.

B. Discussion of Theoretical Results

Several of the most important parametric dependencies are addressed in the following subsections. They correspond to those investigated in the experimental portion of

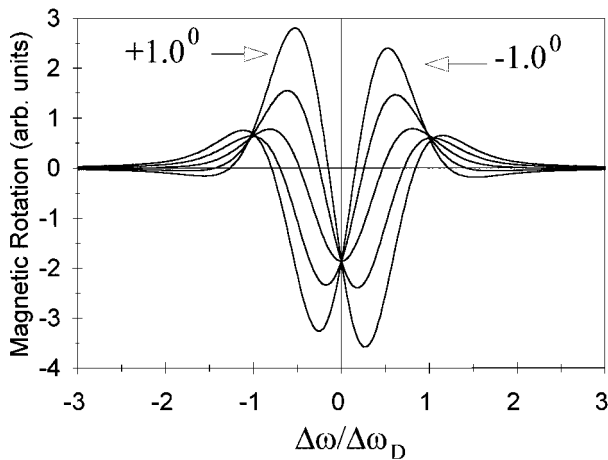


Fig. 3. Theoretical first-derivative curves for the magnetic rotation signal as a function of laser frequency for several analyzer offset angles. The magnetic field was taken to have a value of 45 G and the pressure to be 75 Torr. Values of θ are -1.0° , -0.5° , 0.0° , 0.5° , and 1.0° , where θ is defined in the text.

this paper. Other studies, such as the investigation of various rotational transitions, will be left for future research.

1. Signal versus Polarizer Offset Angle

In Fig. 3 we present plots of the theoretical magnetic rotation spectroscopy signal as a function of laser frequency for various analyzer offset angles. A value of $\theta = 0^\circ$ represents crossed polarizers, but as mentioned above we take into account polarizer imperfections by the factor d/E_0 , which has the value 0.01 for the curves in Fig. 3. Note that there is a qualitative change in shape of the curve as the analyzing polarizer angle changes from an offset on one side of $\theta = 0^\circ$ to the other. These plots represent the cases discussed in subsection 2.A, from which one gains information about either the MCB or the MCD signals. Only at the analyzer setting of $\theta = 0^\circ$ does one probe the effect of magnetic circular dichroism alone. Note as well that the signal is smallest at the $\theta = 0^\circ$ position.

2. Signal versus Magnetic Field Strength

A second parameter of interest is the applied magnetic field. In Fig. 4 are shown several curves for the MRS signal as a function of laser frequency at several magnetic-field strengths. Realistic experimental parameters of $d/E_0 = 0.01$, $P = 50$ Torr, and $\theta = 1.0^\circ$ have been chosen. The steps in B -field strength correspond to those used in the experiment.

For these curves the analyzer offset angle was chosen to be $\theta = 1.0^\circ$, as mentioned above. Other offset angles, specifically $\theta = 0^\circ$, result in the changes discussed in subsection 2.B.1, but the nearly linear dependence of the MRS signal on magnetic field is a constant feature, regardless of the offset angle.

Qualitatively, one would expect that a maximum signal would occur roughly when the Zeeman splitting became comparable with the broadened transition linewidth. Figure 5 shows three curves for magnetic fields such that $\Delta\omega_Z = 1/2\Delta\omega_B$, $\Delta\omega_Z = \Delta\omega_B$, and $\Delta\omega_Z = 2\Delta\omega_B$, illus-

trating such behavior. For a Zeeman splitting larger than $\sim 1/2\Delta\omega_B$ the MRS signal decreases slightly and develops a structure more complicated than that seen at low magnetic fields. These results are still easily explainable by use of the simple heuristic model given in Section 1 when one considers that for large splittings one should see simply the separate effects of LCP and RCP phase shifts, with no mutual overlap.

3. Signal versus Pressure

A final parameter investigated both theoretically and experimentally is the pressure of the gas sample. Figure 6 shows a set of four curves of MRS signal versus frequency for increasing values of the pressure. At low pressures, for which the pressure broadening is much less than the Doppler-broadened width of ≈ 1 GHz, the MRS signal grows with pressure because there are more molecules in

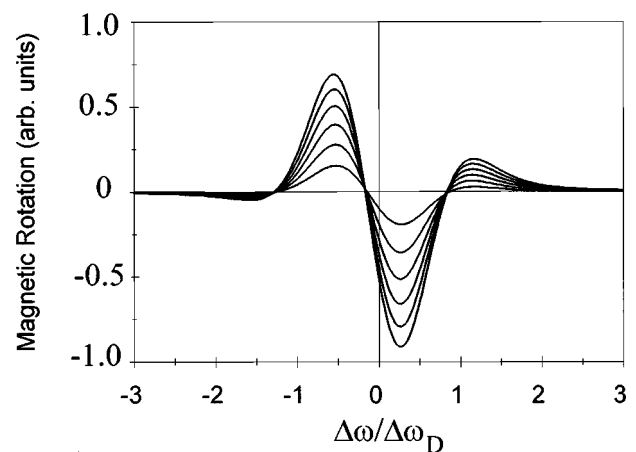


Fig. 4. Theoretical first-derivative curves for the magnetic rotation signal as a function of laser frequency for various magnetic-field strengths. The analyzer offset angle is 1.0° , and the pressure is taken to be 75 Torr. Values of B range from 23 to 138 G in steps of 23 G. The resulting signal amplitude is linear in the applied field for these relatively low fields.

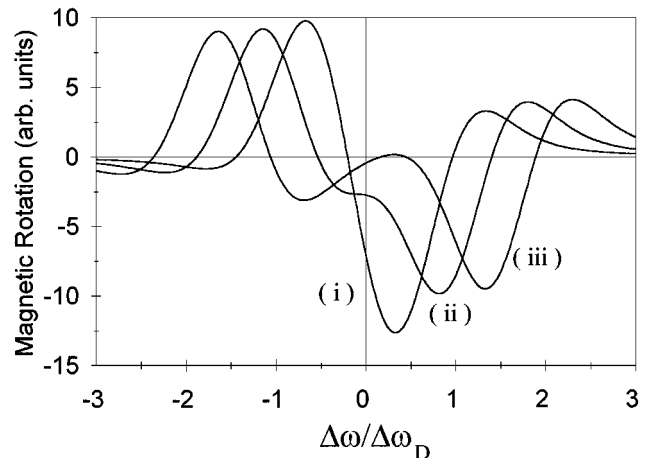


Fig. 5. Theoretical first-derivative curves for the magnetic rotation signal as a function of laser frequency for three widely differing magnetic-field strengths: (i) B is such that the Zeeman splitting is equal to one-half the Doppler width of the transition; (ii) the Zeeman splitting is equal to the Doppler width; (iii) the Zeeman splitting is equal to twice the Doppler width.

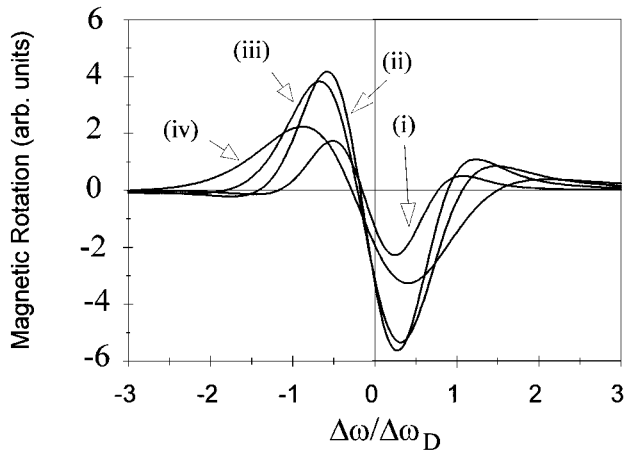


Fig. 6. For $\theta = 1.0^\circ$ the theoretical first-derivative curves for the magnetic rotation signal are plotted as a function of laser frequency for oxygen pressures ranging from 21 Torr (Doppler-broadening-dominated regime) to 420 Torr (pressure-broadening-dominated regime). (i) $P = 21$ Torr, (ii) $P = 105$ Torr, (iii) $P = 210$ Torr, (iv) $P = 420$ Torr. The magnetic field has been taken to be 59 G.

the interaction region, and the linewidth of the signal remains relatively constant. At a pressure somewhat less than that for which the pressure- and Doppler-broadened linewidths are equal (130 and 210 Torr, respectively), the signal amplitude begins to decrease, and the linewidth increases. Qualitatively this is a consequence of the competition between two different processes. In the Doppler limit the strength of interaction depends on the pressure through the total number of atoms, which is linearly proportional to the pressure. When pressure broadening becomes important there is also a dependence on the pressure because the strength of interaction with an individual atom at a given frequency depends on the pressure-broadened width. We find that the signal is overall a decreasing function of pressure in this limit. For all the curves shown in Fig. 6 the analyzer offset angle of $\theta = 1^\circ$ has been chosen, along with a magnetic field of 59 G.

3. EXPERIMENT

Figure 1 is a block diagram of the experimental setup. The diode laser used as a source is a Mitsubishi 4405-01 laser chosen at the time of purchase to have an emission wavelength of 760 nm at $T = 22^\circ\text{C}$. Temperature stabilization to ~ 10 mK is done with a commercial controller (ILX Lightwave LDT-5412). The injection current source is a battery-operated commercial unit (ILX Lightwave LDX-3620). The diode laser has a threshold current of 47 mA and is operated at currents ranging from 60 to 80 mA, depending on the absorption line of interest. Wavelength scanning and modulation of the laser are provided by an external input to the current source. Typical values for the ramp scan of wavelength (H-P 33120A function generator) are 200 mV at a frequency of 100 mHz. A small dither at a frequency of 8–10 kHz and 1.00 V (Tektronix Model CFG280) is attenuated by a factor of 10

(Tektronix 011-0059-02 attenuator) and added to the ramp scan by an operational-amplifier-adding circuit. The resulting output of the operational amplifier is attenuated further by a factor of 2 and fed to the external scan port of the current source, which has been modified to provide a modulation of 0.3 mA/V. Wavelength measurements are made with a wavemeter (Burleigh WA-1000) with a resolution of 0.01 cm^{-1} (0.001 nm) and an absolute accuracy of 1 part in 10^6 .

The Pyrex gas cell is 2.5 cm in diameter and has a length of 40 cm. Two arms at one end are used for filling and pumping and for attachment of a pressure gauge. Pyrex windows are epoxied to the cell body and in the current setup are not antireflection coated. The cell can be evacuated with a cryosorption pump and filled with oxygen gas from a small lecture bottle. The pressure is measured with a linear gauge that permits only approximate measurements, especially at lower pressures of ≤ 25 Torr.

We made a solenoid by closely wrapping 18-gauge coated copper wire onto a 5.0-cm-diameter polyvinyl chloride tube. The total length of the solenoid is 48 cm. A simple calculation shows that the solenoid should provide a magnetic field of 11.7 G/A. We measured the magnetic field independently with a Hall detector (uncalibrated) to determine linearity. The solenoid is driven with a dc power supply (Tenma 72-630). The solenoid is air cooled and could reach a maximum magnetic field of ~ 140 G, limited by the current supply.

The cell is placed inside the solenoid and then between the two polarizers. The first polarizer (as seen by the incident laser) is a broadband polarization beam splitter (Newport 05FC16PB.5). The analyzing polarizer is a Polarcor polarizer mounted in a rotation stage (Newport 481A) that allows for an angular resolution of $\pm 5.0'$. As mounted, the position of minimum transmission (i.e., crossed polarizers) is a setting of $0.0^\circ 25'$ as read from the rotation stage. The extinction ratio of the polarizer pair is $4.2 \pm 0.2 \times 10^{-5}$.

We collect data by first choosing an offset angle for the analyzing polarizer and a fill pressure for the cell after evacuation. The laser frequency is scanned across the oxygen absorption feature, and the lock-in amplifier output signal is recorded on an oscilloscope (H-P 54602A) that can be used in either a single trace or an averaging mode. The trace thus obtained is then saved as a set of voltage-versus-time data points (1000 points per sweep). These data are imported into a commercial spreadsheet program for later analysis. The analysis consists mainly of subtraction of an identical data trace taken with zero magnetic field. In this case, “zero” means that no current is flowing in the solenoid but that the Earth’s magnetic field has not been compensated for.

One final point should be made as to the comparison between the experimental results and the theoretical predictions. The lock-in detection technique gives the freedom of choice of the relative phase used to optimize the signal. In the theoretical treatment we have taken the derivative of the intensity with respect to frequency for comparison. The net result of these two processes is an ambiguity in the overall phase of the predicted versus ex-

perimental signals. We have, however, maintained the same lock-in phase for all measurements.

4. EXPERIMENTAL RESULTS

Here we explore several different parametric dependencies. First, the size and the shape of the magnetic rotation signal as a function of the analyzing polarizer offset angle are addressed. Signal size as a function of magnetic-field strength is addressed next. Then, for a given offset angle, the dependence of the signal's amplitude and shape on oxygen pressure is investigated. In all cases the transition used for the data presented is the $b\ ^1\Sigma_g^+(\nu' = 0, N' = 0, J' = 0) - X\ ^3\Sigma_g^-(\nu'' = 0, N'' = 1, J'' = 1)$ electronic transition. For completeness, we give here as well the Zeeman splitting for the transition above. In the Hund case (b) basis, the Zeeman splitting is given by

$$\begin{aligned} \frac{\delta}{2\pi B} &= \frac{1.001}{J(J+1)} [J(J+1) + S(S+1) \\ &\quad - N(N+1)] M\mu_B \\ &= 1.40 \text{ MHz/G,} \end{aligned}$$

where we have taken $S = 1$, $N = 1$, and $J = 1$ as appropriate for this transition.

A. Signal versus Analyzer Offset Angle

We present here a series of traces for the signal as a function of analyzer offset angle and compare the resulting line shapes with the theoretical model given in Subsection 2.A. We show in Fig. 7 the output of the lock-in amplifier for a series of small polarizer offset angles. Most noticeable is the change in shape of the signal as the offset angle θ is changed from one side of the crossed polarizer setting to the other. All the data sets in Fig. 7 are taken at a magnetic-field strength of 47 G and a pressure of 88 Torr. The behavior displayed does not change qualitatively for other values of magnetic field or pres-

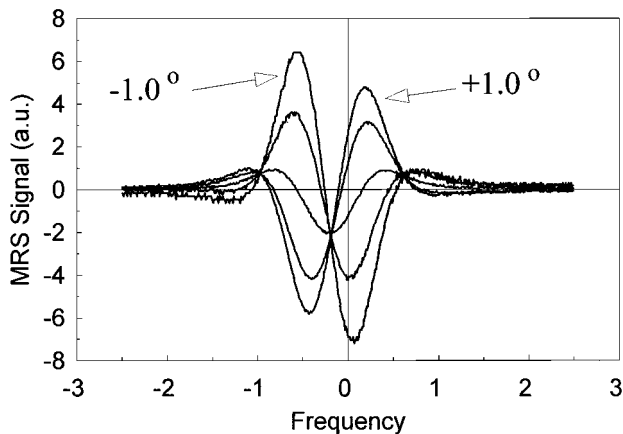


Fig. 7. Experimental results for the magnetic rotation signal as a function of laser frequency for several analyzer settings. Values of θ are -1.0° , -0.5° , 0.0° , and 0.5° , all with an uncertainty of $0^\circ 5'$. The pressure is 88 ± 10 Torr, and the magnetic field is 47 ± 5 G. The signals shown are the output of the lock-in amplifier and represent $1f$ detection, with a subtraction of background run for zero applied magnetic field.

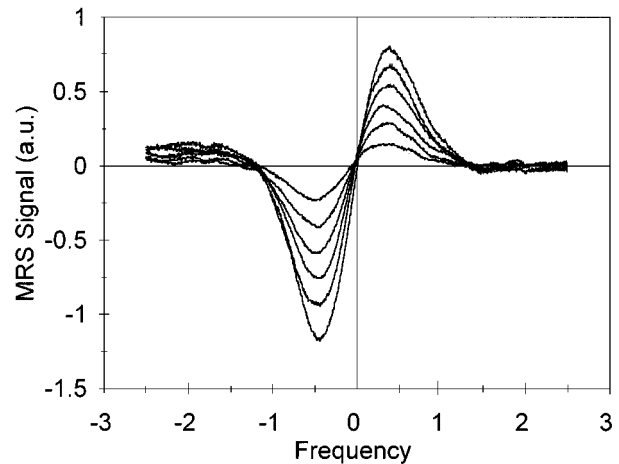


Fig. 8. Experimental results for the magnetic rotation signal for various magnetic-field strengths. The pressure is 75 Torr, and the analyzer offset angle is 1.0° . Signals are the $1f$ lock-in output, with a subtraction of a run with zero applied magnetic field.

sure. In each case in Fig. 7 the curve shown is the result of a subtraction of the zero-magnetic-field trace as explained above.

Because of the uncertainty in determining the offset angle of $\pm 5.0'$, the curves shown in Fig. 7 do not correspond exactly to those in Fig. 3. One could use the theoretical predictions to determine the offset angle by matching curves and using the experimental values of d , magnetic field, and pressure.

In previous research on magnetic rotation spectroscopy there are discussions of the optimum polarizer offset angle to maximize the signal-to-noise ratio. This optimization depends on the remanent transmission of the crossed polarizers.⁷ In one other investigation of this effect an optimum offset angle significantly larger than expected appeared to be found.⁸ For the data shown below at values of θ other than 0° we have chosen an offset angle that approximately maximizes the signal-to-noise ratio, as determined experimentally. We have found that an analyzer angle of approximately 1° gives the best signal-to-noise ratio, defined here as the ratio of the peak-to-peak signal amplitude to the peak-to-peak fluctuations of the signal.

B. Signal versus Magnetic Field

As can be seen from Fig. 4, the growth of the MRS signal as a function of the magnetic-field strength is nearly linear for the relatively low magnetic fields considered here. In Fig. 8 we demonstrate this over a range of magnetic fields from 23 to 140 G. Note the very good qualitative agreement with Fig. 4, including the asymmetry in the curves on either side of the large signal. Figure 9 shows a plot of signal size versus the magnetic-field strength, demonstrating the linear dependence. For the curves shown the analyzer offset angle is $\theta = 1.0^\circ \pm 0.5'$. The pressure is 75 ± 10 Torr. Uncertainty in the magnetic-field strength is ± 5 G. From all curves an identical run with zero applied magnetic field has been subtracted.

C. Signal versus Pressure

Figure 10 shows the MRS signal versus oxygen pressure in the cell for an analyzing polarizer offset angle of θ

$= 1^\circ$. In Fig. 10 there is again a striking qualitative change in the signal as the pressure is increased. A similar dependence was pointed out previously for a slightly different detection method.⁷ It is interesting to note that the signal peak height first increases as a function of pressure because the larger number of molecules present contribute to the magnetic rotation signal. As collision broadening begins to dominate, the signal size begins to decrease, as was discussed in Section 2. In Fig. 11 we plot the signal amplitude (lock-in output, $1f$) as a function of the pressure for data similar to those in Fig. 10. Also in this plot is the theoretical curve for signal amplitude as a function of pressure. The theoretical plot has been scaled to match the size of the experimental signal at the maximum value. For the data points in the plot in Fig. 11 the modulation amplitude has been kept constant for all pressures, which possibly leads to some of the deviation of the experimental data from the theoretical prediction.

The linewidth of the MRS signal as a function of pressure shows linear behavior for pressure above ~ 100 Torr. Below this pressure the linewidth is nearly constant at approximately the Doppler width of 1 GHz.

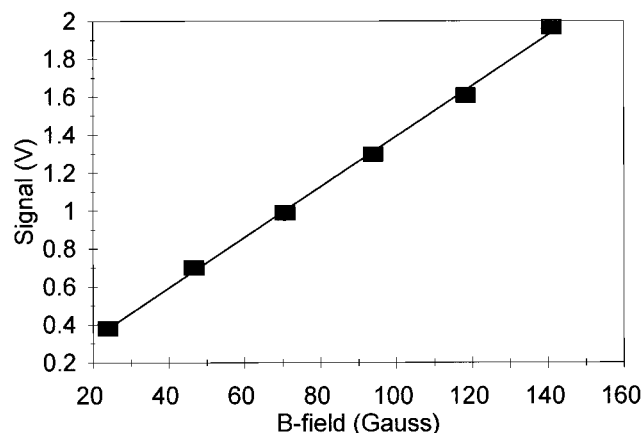


Fig. 9. Plot of the peak-to-peak signal as a function of applied magnetic field with the data in Fig. 8. The solid line is a least-squares straight-line fit to the data.

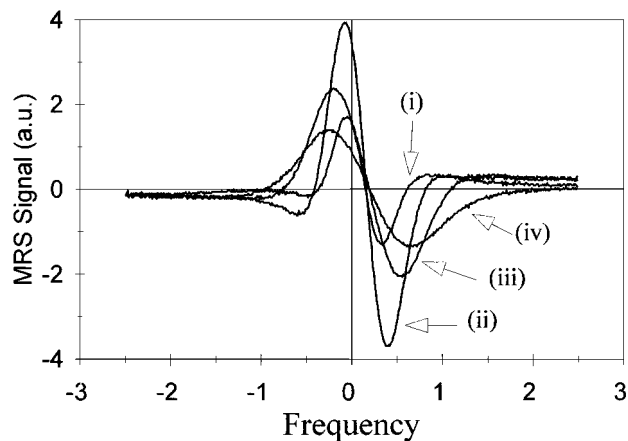


Fig. 10. Lock-in output signal $1f$ as a function of laser frequency for various oxygen pressures. Analyzer offset angle $\theta = 1^\circ$, magnetic-field strength $B = 58$ G. The pressures are (i) 25 Torr, (ii) 100 Torr, (iii) 337 Torr, (iv) 625 Torr.

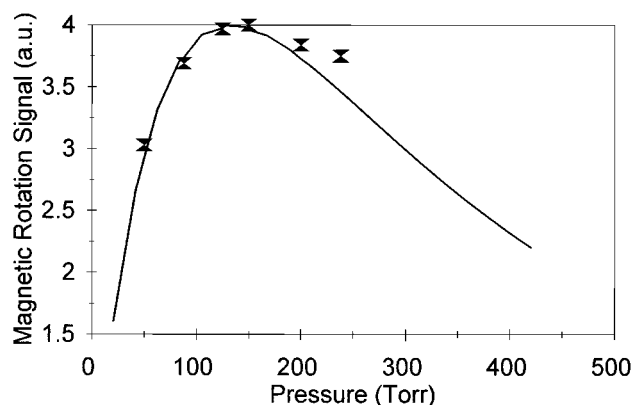


Fig. 11. Plot of the magnetic rotation signal amplitude as a function of pressure for data of Fig. 10. A graph of the theoretical prediction has also been included, with the theory curve scaled to match the experimental one at the maximum signal value.

For data taken at lower pressures we find consistently that the linewidth is such that we can be confident that we are working in a regime of primarily Doppler-broadened oxygen vapor.

5. CONCLUSIONS AND FUTURE RESEARCH

We have presented experimental results for the magnetic rotation spectrum of O_2 , along with a simple theoretical model based on a self-consistent calculation of the magnetization for a sample of molecules used as a source term in Maxwell's equations. The qualitative agreement between theory and experiment is very good. In the course of this study we investigated the signal dependence on several parameters, with special emphasis placed on the magnetic field, pressure, and polarization analyzer offset angle dependence. The last-named parameter permits a separation of MCD and MCB effects.

Future directions of research on this system include more careful study of the rotational quantum number dependence of the MRS signal. In the limit of Hund's case (b), angular momentum coupling, transitions from ground states with angular momentum quantum numbers $J'' = N'' \pm 1$ have a Zeeman splitting that is roughly independent of J , as opposed to the more usual [Hund's case (a)] Zeeman splitting dependence of $1/J(J+1)$. As a function of J the MRS signals for oxygen should therefore also be roughly independent of J . The consequence of large signals for high J quantum numbers would be the possibility of using the magnetic rotation technique as a temperature probe by taking ratios of signals for various transitions and monitoring these as the temperature of the gas sample is varied.

In addition, we have demonstrated that significant signals can be found even at high pressures, specifically, at atmospheric pressure. Thus one could investigate the possibility of inverting the problem as usually posed and use the MRS signal as a magnetic-field probe. This will be another focus of future research.

As mentioned in Section 1, MRS can be 2–3 orders of magnitude more sensitive than modulated absorption

spectroscopy. MRS could thus be used to improve on the bounds recently set for the quantum-mechanical symmetrization postulate.^{14,15}

Finally, the pedagogical aspects of this experiment are not to be ignored. The experimental setup is simple, requiring only a diode laser, one polarizer (for a minimal setup), and a detector (with lock-in amplifier). The diode laser can be externally scanned and modulated with simple function generators. Signals are easily detectable in room air, thus obviating the need even for the glass cell, although such a cell does allow for flexibility. The experiment could conceivably be used in several ways for advanced laboratory experiments, in a fashion similar to the more common investigations of rubidium and cesium vapors.¹⁶

APPENDIX A: CALCULATION OF THE MAGNETIZATION

Consider a three-state system $|a\rangle$, $|b\rangle$, and $|c\rangle$. Let $|a\rangle$ designate the upper state of the system and $|b\rangle$ and $|c\rangle$ designate the lower states of interest. These we will take to be states that are degenerate in the absence of a magnetic field and are split by the Zeeman effect above and below the original degenerate state in the presence of a constant magnetic field. These are the states that couple to level $|a\rangle$ by means of RCP and LCP light. We take the optical input field to have frequency ω and the energy differences between states to be as indicated in Fig. 12.

1. Density Matrix Calculation of the Magnetization

The magnetization of the medium takes the form

$$\mathbf{M} = N\langle\boldsymbol{\mu}\rangle = N \text{Tr}(\rho\boldsymbol{\mu}) = N[\rho_{ab}\langle a|\boldsymbol{\mu}|b\rangle + \rho_{ba}\langle b|\boldsymbol{\mu}|a\rangle + \rho_{ac}\langle a|\boldsymbol{\mu}|c\rangle + \rho_{ca}\langle c|\boldsymbol{\mu}|a\rangle], \quad (\text{A1})$$

where ρ is the density matrix for the atom. The elements of the density matrix are calculated by use of the relation

$$\dot{\rho} = -\frac{i}{\hbar}[H, \rho]. \quad (\text{A2})$$

The Hamiltonian in this case is

$$H = H_A + V_I,$$

where the atomic Hamiltonian has the form

$$H_A = E_a|a\rangle\langle a| + E_b|b\rangle\langle b| + E_c|c\rangle\langle c|$$

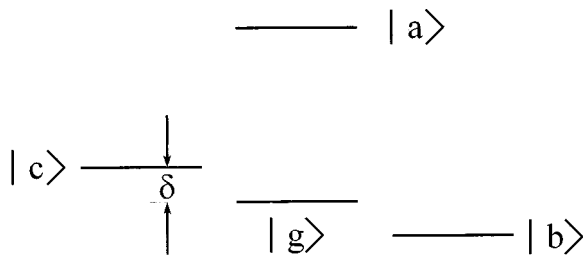


Fig. 12. Schematic of the energy levels used in calculating the magnetization. The triplet ground state consists of two levels that interact with the circularly polarized light, $|b\rangle$ and $|c\rangle$. The unshifted level $|g\rangle$ does not participate in the interaction. The magnetic-field induced frequency shift in the ground-state energy levels is denoted by δ .

and the magnetic dipole interaction Hamiltonian is given by

$$\begin{aligned} V_I &= -\boldsymbol{\mu} \cdot \mathbf{B} \\ &= -\mu B_R \exp(-i\omega t) - \mu B_L \exp(-i\omega t) + \text{H.c.} \\ &\equiv V_{ab}|a\rangle\langle b| + V_{ac}|a\rangle\langle c| + V_{ba}|b\rangle \\ &\quad \times \langle a| + V_{ca}|c\rangle\langle a|. \end{aligned}$$

The electromagnetic (laser) field is presumed to be polarized in the xy plane and propagating along the z direction. Projecting out the relevant off-diagonal density-matrix element of Eq. (A2) and adding a decay term lead to

$$\dot{\rho}_{ab} = -i(\omega_0 - \delta)\rho_{ab} - \gamma\rho_{ab} - \frac{i}{\hbar}V_{ab}(\rho_{bb} - \rho_{aa}), \quad (\text{A3})$$

$$\dot{\rho}_{ac} = -i(\omega_0 + \delta)\rho_{ac} - \gamma\rho_{ac} - \frac{i}{\hbar}V_{ac}(\rho_{cc} - \rho_{aa}). \quad (\text{A4})$$

Taking the electric field to be initially x polarized, we can write the electric and magnetic fields in the form

$$\begin{aligned} \mathbf{E} &= \exp(ikz)\exp(-i\omega t)[E_R\boldsymbol{\epsilon}_R \exp(-i\phi_R) \\ &\quad + E_L\boldsymbol{\epsilon}_L \exp(-i\phi_L)] + \text{c.c.}, \end{aligned} \quad (\text{A5a})$$

$$\begin{aligned} \mathbf{B} &= \exp(ikz)\exp(-i\omega t)[B_R\boldsymbol{\epsilon}_R \exp(-i\phi_R) \\ &\quad + B_L\boldsymbol{\epsilon}_L \exp(-i\phi_L)] + \text{c.c.} \end{aligned} \quad (\text{A5b})$$

Here,

$$B_R = -iE_R/c, \quad B_L = iE_L/c.$$

If state $|c\rangle$ is coupled to the upper state by means of RCP light only and state $|b\rangle$ is coupled to the upper state by LCP light only, the matrix elements of the interaction part of the Hamiltonian become, in the rotating-wave approximation,

$$V_{ab} = \frac{-i\mu E_L}{c} \exp(-i\phi_L)\exp(-i\omega t)\exp(ikz),$$

$$V_{ac} = \frac{i\mu E_R}{c} \exp(-i\phi_R)\exp(-i\omega t)\exp(ikz).$$

Inserting these two equations into Eqs. (A3) and (A4) gives

$$\begin{aligned} \dot{\rho}_{ab} &= -\gamma\rho_{ab} - i(\omega_0 - \delta)\rho_{ab} \\ &\quad - \frac{\mu E_L}{\hbar c} \exp(-i\phi_L)\exp(-i\omega t)\exp(ikz)(\rho_{bb} - \rho_{aa}), \\ \dot{\rho}_{ac} &= -\gamma\rho_{ac} - i(\omega_0 + \delta)\rho_{ac} \\ &\quad + \frac{\mu E_R}{\hbar c} \exp(-i\phi_R)\exp(-i\omega t)\exp(ikz)(\rho_{cc} - \rho_{aa}). \end{aligned} \quad (\text{A6})$$

We take the atomic system to be in the state described by

$$\rho_{aa} = 0, \quad \rho_{bb} = \rho_{cc} = \alpha = \rho_{gg}$$

before the perturbing magnetic field is turned on. In the spirit of first-order perturbation theory (i.e., ignoring power broadening), we use the initial values of the diagonal elements in the equations of motion for the off-diagonal elements of the density matrix. Using these values in Eqs. (A6) and integrating give

$$\begin{aligned}\rho_{ab} &= -\frac{\mu\alpha E_L}{\hbar c} \exp(-i\phi_L)\exp(-i\omega t) \\ &\quad \times \exp(ikz) \frac{\gamma + i[\omega - (\omega_0 - \delta)]}{\gamma^2 + [\omega - (\omega_0 - \delta)]^2}, \\ \rho_{ac} &= +\frac{\mu\alpha E_R}{\hbar c} \exp(-i\phi_R)\exp(-i\omega t) \\ &\quad \times \exp(ikz) \frac{\gamma + i[\omega - (\omega_0 + \delta)]}{\gamma^2 + [\omega - (\omega_0 + \delta)]^2}.\end{aligned}$$

Inserting these two equations into Eq. (A1) leads to the macroscopic magnetization

$$\begin{aligned}\mathbf{M} &= N \frac{\mu^2\alpha}{\hbar c} \exp[i(kz - \omega t)] \\ &\quad \times \left\{ E_R \frac{\gamma + i[\omega(\omega_0 + \delta)]}{\gamma^2 + [\omega - (\omega_0 + \delta)]^2} \exp(-i\phi_R)\boldsymbol{\epsilon}_R \right. \\ &\quad \left. - E_L \frac{\gamma + i[\omega - (\omega_0 - \delta)]}{\gamma^2 + [\omega - (\omega_0 - \delta)]^2} \exp(-i\phi_L)\boldsymbol{\epsilon}_L \right\} + \text{c.c.}\end{aligned}$$

For convenience, we define

$$\begin{aligned}\mathbf{M} &= M_L\boldsymbol{\epsilon}_L \exp[i(kz - \omega t)]\exp(-i\phi_L) \\ &\quad + M_R\boldsymbol{\epsilon}_R \exp[i(kz - \omega t)]\exp(-i\phi_R).\end{aligned}$$

Here,

$$M_R = N \frac{\mu^2\alpha E_R}{\hbar c} \frac{\gamma + i(\omega - \omega_R)}{\gamma^2 + (\omega - \omega_R)^2}, \quad (\text{A7a})$$

$$M_L = -N \frac{\mu^2\alpha E_L}{\hbar c} \frac{\gamma + i(\omega - \omega_L)}{\gamma^2 + (\omega - \omega_L)^2}, \quad (\text{A7b})$$

with $\omega_{R,L} = \omega_0 \pm \delta$.

2. Insertion of Magnetization into the Wave Equation

Using Eqs. (A5) and (A7) in the wave equation [Eq. (1)] and making the usual slowly varying phase and amplitude approximations lead to the following equations, which are valid for a temporal steady state:

$$\frac{\partial\phi_{R,L}}{\partial z} = \frac{\mu_0\omega}{2E_{R,L}} \text{Im}(M_{R,L}),$$

$$\frac{\partial E_{R,L}}{\partial z} = -\frac{\mu_0\omega}{2} \text{Re}(M_{R,L}).$$

Using Eqs. (A7) and integrating these relations across the cell taken to have length l give

$$\phi_{R,L}(l) = \kappa F_{R,L}(\omega, \omega_{R,L}),$$

$$E_{R,L} = E_0 \exp[-\kappa G_{R,L}(\omega, \omega_{R,L})].$$

Here,

$$\kappa = \frac{N\mu_0\mu^2 c \alpha}{2\hbar} l,$$

$$F_{R,L}(\omega, \omega_{R,L}) = \frac{\omega(\omega - \omega_{R,L})}{\gamma^2 + (\omega - \omega_{R,L})^2}, \quad (\text{A8})$$

$$G_{R,L}(\omega, \omega_{R,L}) = \frac{\omega\gamma}{\gamma^2 + (\omega - \omega_{R,L})^2}. \quad (\text{A9})$$

3. Doppler Broadening

The expressions derived in the preceding subsection are valid for a homogeneously broadened linewidth. In the experimental setup the dominant mechanism that leads to homogeneous broadening is pressure broadening. The parameter γ can be taken to be the pressure-broadened linewidth. To include the effects of Doppler broadening, Eqs. (A8) and (A9) should be multiplied by the Gaussian weighting factor

$$W(\omega', \omega_{R,L}) = \frac{1}{\sqrt{\pi}\Delta\omega} \exp[-(\omega', \omega_{R,L})^2/\Delta\omega^2].$$

That is, $F_{R,L}$ and $G_{R,L}$ in Eqs. (A8) and (A9) should be replaced by

$$\begin{aligned}f_{R,L} &\equiv \int_{-\infty}^{\infty} W(\omega, \omega_{R,L}) F_{R,L}(\omega, \omega') d\omega' \\ &= \int_{-\infty}^{\infty} \frac{1}{\sqrt{\pi}\Delta\omega} \exp[-(\omega' - \omega_{R,L})^2/\Delta\omega^2] \\ &\quad \times \frac{\omega(\omega - \omega')}{\gamma^2 + (\omega - \omega')^2} d\omega', \\ g_{R,L} &\equiv \int_{-\infty}^{\infty} W(\omega', \omega_{R,L}) G_{R,L}(\omega, \omega') d\omega' \\ &= \int_{-\infty}^{\infty} \frac{1}{\sqrt{\pi}\Delta\omega} \exp[-(\omega' - \omega_{R,L})^2/\Delta\omega^2] \\ &\quad \times \frac{\omega\gamma}{\gamma^2 + (\omega - \omega')^2} d\omega'.\end{aligned}$$

These relations are Eqs. (4).

ACKNOWLEDGMENT

This research has been made possible by support from the Research Corporation in the form of a Cottrell Science Award to R. J. Brechia.

REFERENCES

1. A. D. Buckingham and P. J. Stephens, "Magnetic optical activity," *Ann. Rev. Phys. Chem.* **17**, 399–432 (1966).
2. G. A. Mann and C. D. Hause, "Magnetic rotation spectra of nitric oxide in the near infrared," *J. Chem. Phys.* **33**, 1117–1123 (1960).
3. J. L. Aubel and C. D. Hause, "Magnetic rotation spectra of the 2–0 vibration–rotation band of NO," *J. Chem. Phys.* **44**, 2659–2664 (1966).
4. D. B. Keck and C. D. Hause, "Spectra of the 1–0 vibration–

- rotation band of nitric oxide," *J. Chem. Phys.* **49**, 3458–3464 (1968).
5. A. D. Buckingham and G. A. Segal, "Calculation of the magnetic rotation spectra of NO in the near infrared," *J. Chem. Phys.* **49**, 1964–1966 (1968).
 6. F. A. Blum, K. W. Nill, and A. J. Strauss, "Line shape of the Doppler-limited infrared magnetic rotation spectrum of nitric oxide," *J. Chem. Phys.* **58**, 4968–4970 (1973).
 7. G. Litfin, C. R. Pollock, R. F. Curl, Jr., and F. K. Tittel, "Sensitive enhancement of laser absorption spectroscopy by magnetic rotation effect," *J. Chem. Phys.* **72**, 6602–6605 (1980).
 8. T. A. Blake, C. Chackerian, Jr., and J. R. Podolske, "Prognosis for a mid-infrared magnetic rotation spectrometer for the *in situ* detection of atmospheric free radicals," *Appl. Opt.* **35**, 973–985 (1996).
 9. A. F. Stalder and W. H. Eberhardt, "Magnetically induced circular dichroism and birefringence in single lines of the electronic spectrum of ICl," *J. Chem. Phys.* **47**, 1445–1451 (1967).
 10. M. C. McCarthy, J. C. Bloch, and R. W. Field, "Frequency-modulation enhanced magnetic rotation spectroscopy: a sensitive and selective absorption scheme for paramagnetic molecules," *J. Chem. Phys.* **100**, 6331–6346 (1994).
 11. M. C. McCarthy and R. W. Field, "Frequency-modulation enhanced magnetic rotation spectroscopy of PdH, PdD, NiH and CuH," *J. Chem. Phys.* **100**, 6347–6358 (1994).
 12. M. C. McCarthy and R. W. Field, "The use of magnetic rotation spectroscopy to simplify and presort spectra: an application to NiH and CeF," *J. Chem. Phys.* **96**, 7237–7244 (1992).
 13. M. Sargent III, M. O. Scully, and W. E. Lamb, Jr., *Laser Physics* (Addison-Wesley, Reading, Mass., 1974), pp. 372–375.
 14. M. De Angelis, G. Gagliardi, L. Gianfrini, and G. M. Tino, "Test of the symmetrization postulate for spin-0 particles," *Phys. Rev. Lett.* **76**, 2840–2843 (1996).
 15. R. C. Hilborn and C. L. Yuca, "Spectroscopic test of the symmetrization postulate for spin-0 nuclei," *Phys. Rev. Lett.* **76**, 2844–2847 (1996).
 16. D. A. Van Baak, "Resonant Faraday rotation as a probe of atomic dispersion," *Am. J. Phys.* **64**, 724–735 (1996).